Proteopathy Linked to Exon-Skipping Isoform of RGR-Opsin Contributes to the Pathogenesis of Age-Related Macular Degeneration

Chi Ren,[1,2] Haoran Cui,[1–3] Xuan Bao,[1,2,4] Lvzhen Huang,[1,2] Shikun He,[5] Henry K. W. Fong,[5,6] and Mingwei Zhao[1,2]

[1]Department of Ophthalmology, Eye Disease and Optometry Institute, Peking University People's Hospital, Beijing, China
[2]Beijing Key Laboratory of Diagnosis and Therapy of Retinal and Choroid Diseases, Beijing, China
[3]Department of Ophthalmology, Beijing Chaoyang Hospital, Capital Medical University, Beijing, China
[4]Department of Molecular and Human Genetics, Baylor College of Medicine, Houston, Texas, United States
[5]Department of Ophthalmology, USC Roski Eye Institute, Keck School of Medicine of University of Southern California, Los Angeles, California, United States
[6]Department of Molecular Microbiology and Immunology, University of Southern California, Los Angeles, California, United States

Correspondence: Henry K.W. Fong, Department of Ophthalmology, Keck School of Medicine of University of Southern California, Mudd Memorial Research Bldg, MMR-322, 1333 San Pablo St., Los Angeles, CA 90089, USA;
hfong@usc.edu.
Mingwei Zhao, Department of Ophthalmology, Eye Disease and Optometry Institute, Peking University People's Hospital, Beijing, China; Beijing Key Laboratory of Diagnosis and Therapy of Retinal and Choroid Diseases, Beijing, China; Xizhimen South Street 11, Xi Cheng District, Beijing 100044, China;
dr_zhaomingwei@163.com.

CR and HC contributed equally to this work.

Received: August 10, 2023
Accepted: October 9, 2023
Published: October 26, 2023

Citation: Ren C, Cui H, Bao X, et al. Proteopathy linked to exon-skipping isoform of RGR-Opsin contributes to the pathogenesis of age-related macular degeneration. *Invest Ophthalmol Vis Sci.* 2023;64(13):41. https://doi.org/10.1167/iovs.64.13.41

Purpose. Proteopathy is believed to contribute to age-related macular degeneration (AMD). Much research indicates that AMD begins in the retinal pigment epithelium (RPE), which is associated with formation of extracellular drusen, a clinical hallmark of AMD. Human RPE produces a drusen-associated abnormal protein, the exon VI-skipping splice isoform of retinal G protein-coupled receptor (RGR-d). In this study, we investigate the detrimental effects of RGR-d on cultured cells and mouse retina.

Methods. ARPE-19 cells were stably infected by lentivirus overexpressing RGR or RGR-d and were treated with MG132, sometimes combined with or without endoplasmic reticulum (ER) stress inducer, tunicamycin. RGR and RGR-d protein expression, degeneration pathway, and potential cytotoxicity were explored. Homozygous RGR-d mice aged 8 or 14 months were fed with a high-fat diet for 3 months and then subjected to ocular examination and histopathology experiments.

Results. We confirm that RGR-d is proteotoxic under various conditions. In ARPE-19 cells, RGR-d is misfolded and almost completely degraded via the ubiquitin-proteasome system. Unlike normal RGR, RGR-d increases ER stress, triggers the unfolded protein response, and exerts potent cytotoxicity. Aged RGR-d mice manifest disrupted RPE cell integrity, apoptotic photoreceptors, choroidal deposition of complement C3, and $CD86^{+}CD32^{+}$ proinflammatory cell infiltration into retina and RPE–choroid. Furthermore, the AMD-like phenotype of RGR-d mice can be aggravated by a high-fat diet.

Conclusions. Our study confirmed the pathogenicity of the RGR splice isoform and corroborated a significant role of proteopathy in AMD. These findings may contribute to greater comprehension of the multifactorial causes of AMD.

Keywords: age-related macular degeneration, drusen, retinal pigment epithelium, RGR-d, proteopathy, endoplasmic reticulum stress

Abnormal protein deposits at extracellular or intracellular sites are a feature of numerous neurodegenerative diseases such as Parkinson disease, Alzheimer disease, and age-related macular degeneration (AMD).[1–3] Drusen, extracellular deposits immediately beneath the retinal pigmental epithelium (RPE) in human eyes, develop commonly with aging.[4,5]

To date, the pathogenetic mechanism underlying drusen formation has yet to be completely uncovered. Increasing evidence advocates that proteopathy plays a significant role in AMD and that AMD may be a protein misfolding disease.[6–8] Various cellular insults, such as oxidative stress, hypoxia, and gene mutations, can lead to misfolded or unfolded protein accumulation in the endoplasmic reticulum (ER), which may be cytotoxic if left unchecked.[9,10] Dynamic and self-regulating quality control systems, including the ubiquitin-proteasome system (UPS) and autophagy, are critical for maintaining protein homeostasis and relieving

prolonged impairment.[11] It is believed that the RPE participates in this process,[12–15] in which abnormalities may occur in protein synthesis and quality control systems due to multiple pathologic factors upon aging that lead to abnormal protein accumulation and sub-RPE deposits.

One trackable drusen-associated abnormal protein expressed by RPE is the exon VI-skipping splice isoform of retinal G protein-coupled receptor (RGR), referred to as RGR-d (NP_001012740).[16–18] RGR is a nonvisual opsin that serves to maintain sufficient synthesis of 11-*cis*-retinal during light and dark alternation.[19–21] RGR-d may have no such function, since it is unlikely to fold correctly into functional structure due to lack of the entire transmembrane domain VI of RGR.[22] RGR-d, or a fragment thereof, is released by RPE and deposited into Bruch's membrane and, notably, exists in both hard and soft drusen in human donor eyes.[20,23] Our recent study of old homozygous RGR-d mice identified a high pathogenicity of RGR-d for degeneration of the choriocapillaris, RPE, and photoreceptors, with drusen-like deposits in sub-RPE space and along Bruch's membrane.[22]

Despite current evidence pointing to a link between the abnormal RGR isoform and AMD pathogenesis, there is a scarcity of information regarding RGR-d protein processing behavior and mechanisms of underlying cellular damage. Hence, we conducted studies using the ARPE-19 cell line and aging RGR-d mice to further reveal the impact and mechanism of RGR-d proteopathy in AMD-like phenotypes.

Materials and Methods

Lentivirus Construction and Cell Infection

Lentivirus carrying the human *RGR* and *RGR-d* gene (Lv-RGR and Lv-RGR-d) was constructed commercially by Genechem Technology (Shanghai, China). In brief, the coding sequences of RGR and RGR-d were obtained by polymerase chain reaction (PCR) with specific primers flanked with PacI and NheI recognition sites. The templates and primers are listed in Table 1. The products were gel-purified, digested, inserted into the plasmid vector (CMV-MCS-3FLAG-SV40-puromycin), and further identified by sequencing. For production of lentivirus, 293T packaging cells were transfected with vector plasmids (internal control) or plasmids carrying the *RGR* or *RGR-d* gene as well as both pHelper 1.0 and pHelper2.0 plasmids. Seventy-two hours after cell transfection, the culture media containing lentivirus were collected, filtered, and centrifuged (25,000 rpm, 2 hours, 4°C), and purified lentivirus was titered.

Cell Culture and Treatment

ARPE-19 cells were purchased from the Chinese Academy of Sciences Cell Bank (Shanghai, China) and maintained as previously described.[24] Stable cell lines were established by lentivirus infection (multiplicity of infection (MOI) = 5) for 24 hours, followed by puromycin (2 µg/mL) selection for 2 weeks. In some studies, cells were treated with dimethyl sulfoxide (DMSO) (D12345; Invitrogen, Carlsbad, CA, USA) or MG132 (ab141003; Abcam, Cambridge, MA, USA) for different time durations. For assessments of changes in autophagy flux, we treated the cells with 2 µM MG132 combined with or without 50 nM bafilomycin A1 (BafA1) (ab120497; Abcam) for 12 hours. For investigations of ER stress and unfolded protein response (UPR) pathways, cells were treated with 2 µM MG132 combined with or without 5 µg/mL tunicamycin (TM) (ab120296; Abcam) for 16 hours.

Quantitative Reverse Transcription PCR

Total RNA of cells was extracted using the RNA extraction kit (Omega Bio-Tek, Guangzhou, China) and used to synthesize cDNA with a reverse transcription kit (TOYOBO, Shanghai, China). Quantitative real-time PCR reactions were performed using SYBR Green qPCR reagents (TOYOBO). The primer sequences are listed in Table 1.

Western Blotting Assays

Proteins were electrophoresed in a 10% NuPAGE Bis-Tris gel (NP0303BOX; Invitrogen) and then transferred to a nitrocellulose membrane (Millipore, Billerica, MA, USA). The blots were incubated with the indicated primary antibodies (4°C, overnight) and then with a secondary antibody (room temperature, 1 hour). The antibodies are listed in Table 2. The bands were visualized with a near-infrared system (Odessey; LI-COR, Lincoln, NE, USA).

Immunocolocalization Assay

Immunocolocalization staining was carried out as before.[22] The primary and secondary antibodies are listed in Table 2. The stained slides were finally observed on a TCS-SP5 confocal microscope (Leica, Wetzlar, Germany). For

Table 1. Primers Used for PCR

Gene	Primer	
Template acquisition for lentivirus construction		
RGR (NM_002921)	Forward:	GATCCAGTTTGGTTAATTAACGTTACATAACTTACGGTAAATGGCCCGCCTGGCTG
	Reverse:	AATGCCAACTCTGAGCTTCTTGGTTCGGTCCTTCTCCCTCTTC
RGR-d (NM_001012722)	Forward:	GATCCAGTTTGGTTAATTAACGCCACCCGTTACATAACTTACGGTAAATGGCCCGCC TGGCTG
	Reverse:	AATGCCAACTCTGAGCTTCTTGGTTCGGTCCTTCTCCCTCTTC
Quantitative reverse transcription PCR		
GAPDH	Forward:	GTCTCCTCTGACTTCAACAGCG
	Reverse:	ACCACCCTGTTGCTGTAGCCAA
RGR	Forward:	ATGGTGCTACTGGTGGAAGC
	Reverse:	CTGTGGGAGACACGGAGAAG
RGR-d	Forward:	GTGGCCATCTCCAGGTGC
	Reverse:	GAAGGTGGGTGAGTG TCTGG

Investigative Ophthalmology & Visual Science

Table 2. Antibodies Used in the Study

Antibody	Source	Identifier
Primary antibodies used in Western blotting		
Mouse anti–β actin (1:5000)	Abcam, Cambridge, MA, USA	Cat# ab8226
Rabbit anti-DDDK tag (1:1000)	Abcam, Cambridge, MA, USA	Cat# ab205606
Rabbit anti-LC3b (1:1000)	Abcam, Cambridge, MA, USA	Cat# ab192890
Rabbit anti-SQSTM1/p62 (1:1000)	ProteinTech, Wuhan, China	Cat# 18420-1-AP
Rabbit anti-calnexin (1:1000)	Abcam, Cambridge, MA, USA	Cat# ab22595
Rabbit anti-GRP78 (1:1000)	Abcam, Cambridge, MA, USA	Cat# ab108613
Rabbit anti-IRE1α (1:1000)	Cell Signaling Technology, Boston, USA	Cat# 3294T
Rabbit anti-IRE1 (phospho S724) (1:500)	Abcam, Cambridge, MA, USA	Cat# ab48187
Rabbit anti-ATF6 (1:1000)	Cell Signaling Technology, Boston, MA, USA	Cat# 65880T
Rabbit anti-ATF4 (1:1000)	Abcam, Cambridge, MA, USA	Cat# ab184909
Rabbit anti-PERK (1:1000)	Cell Signaling Technology, Boston, MA, USA	Cat# 3192S
Mouse anti-CHOP (1:500)	Cell Signaling Technology, Boston, MA, USA	Cat# 2895S
Mouse anti-HA tag (1:1000)	LABLEAD, Beijing, China	Cat# H1003
Secondary antibodies used in Western blotting		
CruzFluor 790–conjugated mouse IgG kappa light chain binding protein (m-IgGk BP) (1:5000)	Santa Cruz, Santa Cruz, CA, USA	Cat# sc-516181
CruzFluor 790–conjugated mouse anti-rabbit IgG (1:5000)	Santa Cruz, Santa Cruz, CA, USA	Cat# sc-516253
Primary antibodies used in immunocolocalization assay		
Rabbit anti-DDDK tag (1:100)	Abcam, Cambridge, MA, USA	Cat# ab205606
Mouse anti-Flag (1:100)	Sigma-Aldrich, St. Louis, MO, USA	Cat# F3165
Rabbit anti-calnexin (1:100)	Abcam, Cambridge, MA, USA	Cat# ab22595
Rabbit anti-GM130 (1:100)	Abcam, Cambridge, MA, USA	Cat# ab52649
Mouse anti-LAMP2 (1:100)	Abcam, Cambridge, MA, USA	Cat# ab25631
Rabbit anti-RAB7 (1:100)	Abcam, Cambridge, MA, USA	Cat# ab137029
Secondary antibodies used in immunofluorescence staining		
Alexa Fluor 488–conjugated goat anti-rabbit IgG H&L (1:1000)	Abcam, Cambridge, MA, USA	Cat# ab150077
Alexa Fluor 488–conjugated goat anti-mouse IgG H&L (1:1000)	Abcam, Cambridge, MA, USA	Cat# ab150113
Alexa Fluor 594–conjugated goat anti-mouse IgG H&L (1:1000)	Abcam, Cambridge, MA, USA	Cat# ab150116
Alexa Fluor 594–conjugated goat anti-rabbit IgG H&L (1:1000)	Abcam, Cambridge, MA, USA	Cat# ab150080
Primary antibodies used in flow cytometry		
APC/Fire 750 anti-mouse CD45 (0.25 µg per 10^6 cells in 100 µL)	BioLegend, San Diego, CA, USA	Cat# 103153
Alexa Fluor 488 anti-human/mouse CD11b (0.25 µg per 10^6 cells in 100 µL)	BioLegend, San Diego, CA, USA	Cat# 101219
PE/Cyanine7 anti-mouse CD86 (1.0 µg per 10^6 cells in 100 µL)	BioLegend, San Diego, CA, USA	Cat# 105013
Brilliant Violet 421 anti-mouse CD206 (5 µL per 10^6 cells in 100 µL)	BioLegend, San Diego, CA, USA	Cat# 141717
APC anti-mouse CD32 (1.0 µg per 10^6 cells in 100 µL)	BioLegend, San Diego, CA, USA	Cat# 156405
PE anti-mouse CD163 (0.25 µg per 10^6 cells in 100 µL)	BioLegend, San Diego, CA, USA	Cat# 155307

quantitative analysis of colocalization, Pearson's correlation coefficients were calculated using the Coloc 2 plugin in Fiji/ImageJ following the instructions provided on the Coloc 2 website (https://imagej.net/plugins/coloc-2). Regions of interest were chosen on the cytoplasm.

Cell Transfection and Coimmunoprecipitation Assay

The stably transfected cell lines went through transient transfection with the HA-Ubiquitin (HA-Ub) plasmid (Youbio, Changsha, China), using a DNA transfection reagent (Lipofectamine 3000; Invitrogen) according to the manufacturer's instructions. After being treated with DMSO or 2 µM MG132 for 16 hours, the cells were lysed in immunoprecipitation (IP) lysis/wash buffer (LABLEAD, Beijing, China) supplement with protease inhibitor, then incubated with precoated Flag- or Myc-magnetic beads (LABLEAD) for 1 hour at 4°C on a rotator. The Myc-magnetic beads served as a negative control. The manufacturer's protocol was followed to wash the beads and elute the protein complex, which was subjected to Western blotting to detect the HA signal.

Cell Cycle Distribution and Apoptosis Determination

Cell cycle and apoptosis were determined using the cell cycle assay kit (Solarbio, Beijing, China) and Annexin V-FITC apoptosis detection kit (BD Biosciences, San Jose, CA, USA), according to the manufacturers' instructions. The prepared cells were subjected to FACSCalibur flow cytometer (BD Biosciences), and the results were analyzed using ModFit LT software (Verity Software House, Topsham, ME, USA).

EdU Proliferation Assay

The cells were seeded onto 96-well plates at 3×10^3 cells/well and treated with 2 µM MG132 combined with or without 5 µg/mL TM for 12 hours. A Click-iT EdU assay kit (LABLEAD) was used for cell proliferation detec-

Investigative Ophthalmology & Visual Science

tion. Cells were incubated with 10 µM EdU for 4 hours and fixed for 15 minutes in 4% paraformaldehyde (PFA) at room temperature. EdU staining was then performed using the YF 488 Azide according to the manufacturer's instructions and finally observed under an Olympus U-RFL-T fluorescence microscope (Olympus, Tokyo, Japan).

Cell Growth

The cells were seeded onto 24-well plates at 5×10^4 cells/well. The numbers of cells were counted for 7 consecutive days using a hemocytometer under a light microscope, and the cell growth curves were plotted.

Cell Viability

The cells were seeded onto 96-well plates at $\geq 5 \times 10^3$ cells/well and treated with MG132 of different concentrations for 12 hours. CCK-8 dye (Dojindo, Shanghai, China) was added to cells, and absorbance at 450 nm was measured after 2 hours.

Animals

Wild-type (WT) and homozygous RGR-d mice (genetic background: B6D2F1/J; Jackson Laboratory, Bar Harbor, ME, USA) were used in this study. Homozygous RGR-d mice were generated as described previously.[22] All procedures were approved by the Animal Use and Ethical Committee of Peking University People's Hospital (no. 2019PHC027), and experiments were conducted according to the ARVO Statement of Animal Use. Some WT and RGR-d mice began the high-fat diet (HFD) (D12079B; Research Diets, New Brunswick, NJ, USA) at 8 or 14 months old for 3 months. AIN-93M (D10012M; Research Diets) diet was used as a standard diet.

Staining of RPE-Choroid Flat Mounts

Mouse RPE–choroid flat mounts were isolated, fixed with 4% PFA, blocked with 1% BSA, and stained with rabbit anti–ZO-1 antibody (Table 2). Immunofluorescent staining was visualized with Alexa Fluor 594–labeled secondary antibody (ab150080; Abcam). All images were obtained using the TCS-SP8 DIVE confocal microscope (Leica).

TUNEL Assay

Mouse eyes were dehydrated, embedded in paraffin, sectioned at 6 µm thickness, and subjected toTUNEL assay using an in situ cell death detection kit (Roche, Mannheim, Germany), according to the manufacturer's instructions. The slides were scanned with a Panoramic slide scanner at ×40 magnification (3DHISTECH, Budapest, Hungary) and visualized by CaseViewer software (3DHISTECH).

Ocular Histology

Formalin-fixed, paraffin-embedded sections of mouse eyes were stained with a hematoxylin and eosin (HE) staining kit (Beyotime, Shanghai, China) according to the manufacturer's instructions. Digital images were acquired using a Nanozoomer Digital Pathology (NDP) Scanner (Hamamatsu, Japan).

Frozen Section Preparation and Immunofluorescence

Frozen section preparation and immunofluorescence of mouse eyecups were prepared as previously described.[22] After permeabilization and blocking, the sections were incubated at 4°C with the anti–complement C3 antibody (PA5-21349; Invitrogen) or anti–glial fibrillary acidic protein (GFAP) antibody (ab207165; Abcam) overnight and then with a corresponding secondary antibody (Table 2) for 1 hour. The C3 staining was visualized with the Zeiss LSM 780 confocal microscope (Zeiss, Oberkochen, Germany). The GFAP staining was scanned with a Panoramic slide scanner at ×40 magnification (3DHISTECH) and visualized by CaseViewer software (3DHISTECH).

Flow Cytometry for Retina and RPE-Choroid

Tissues from eight mouse eyes were pooled to obtain sufficient cell numbers. Retinas and RPE–choroid complexes were isolated by dissection and digested at 37°C for 20 minutes in 1 mg/mL collagenase D solution, including 2% FBS (Gibco, Waltham, MA, USA), 10 mM HEPES (Invitrogen), and 100 U/mL DNAse1 (Beyotime) in Hank's balanced salt solution (Gibco), followed by filtering through a 70-µm cell strainer and blocked with Fc-block reagent (156603; BioLegend, San Diego, CA, USA). The samples were stained for cell viability and labeled with indicated primary antibodies (Table 2). Flow cytometry was performed on a FACS Calibur flow cytometer (BD Biosciences) and analyzed with software (FlowJo, Ashland, OR, USA).

Fundus Color Photography and Optical Coherence Tomography Examination

In some experiments, mice of different ages were fed with an AIN-93M or high-fat diet for 3 months. Afterward, they were subject to optical coherence tomography (OCT) (isOCT; 4D-ISOCT Optoprobe, Burnaby, Canada) and fundus color photography (OPTO-RIS; Optoprobe Science). The mice were examined under anesthesia with an intraperitoneal injection of 2.5% tribromoethanol (Sigma-Aldrich, Missouri, MO, USA), as described previously.[25]

Transmission Electron Microscopy

After 3 months of standard (AIN-93M) or high-fat diet (Western diet), the mice were euthanized and the eyes were fixed in 2.5% glutaraldehyde (Solarbio), followed by 1% osmium tetroxide (Electron Microscopy Sciences, Hatfield, PA, USA) fixation, ferrous oxide reduction, and uranyl acetate staining. The samples were subsequently dehydrated and then embedded in Eponate 12 resin (Ted Pella, Redding, CA, USA). Fundus sections were obtained and contrasted with uranyl acetate and lead citrate. Finally, the samples were observed using a transmission electron telescope (JEM-2100; JEOL, Peabody, MA, USA).

Statistical Analysis

Two-tailed Student's *t*-test was used to assess differences between two groups. Differences among multiple groups were evaluated using one-way ANOVA followed by Fisher's least significant difference post hoc test. Statistical

Investigative Ophthalmology & Visual Science

significance was determined by $P < 0.05$ ($^{*}P < 0.05$, $^{**}P < 0.01$, $^{***}P < 0.001$).

Results

Degradation of Misfolded RGR-d Protein by the Ubiquitin-Proteasome System

Stably transfected cells that overexpressed Flag-tagged human *RGR* and *RGR-d* proteins, referred to as RGR cells and RGR-d cells, respectively, were used for the following investigations. Quantitative PCR confirmed several hundred-fold increases in mRNA expression of both RGR and RGR-d transcripts (Fig. 1A). Contrarily, the RGR-d protein was detected at extremely low levels, while RGR was abundantly expressed under the same culture conditions (Figs. 1B–D). After treatment with 4 µM MG132, a 26S proteasome inhibitor, the RGR-d protein accumulated in a time-dependent pattern (Figs. 1B, 1C), and both RGR and RGR-d tended to distribute toward the perinuclear region (Fig. 1D). Co-IP assay revealed a significant increase in the level of polyubiquitin chains on RGR-d compared to RGR in ARPE-19 cells (Fig. 1E). These results showed that although successfully translated from mRNA, the misfolded RGR-d protein was almost completely degraded by the UPS under normal culture conditions.

Mislocalization and Processing Behavior of RGR-d Protein

We treated both RGR and RGR-d cells with 2 µM MG132 for 16 hours to achieve enrichment of the proteins. Figure 2 showed representative results of immunofluorescence double-labeling of Flag-tag and markers for organelles, including calnexin for ER (Fig. 2A), Golgi matrix protein 130 kD (GM130) for Golgi apparatus (Fig. 2B), lysosomal-associated membrane protein 2 (LAMP2) for lysosomes (Fig. 2C), and Rab7, the key protein for autophagosome and lysosome fusion process (Fig. 2D). RGR colocalized well with calnexin and GM130, while RGR-d showed a significantly weaker relationship (Fig. 2E), suggesting divergence from RGR and an aberrant process of protein folding in the ER and modification in the Golgi apparatus for RGR-d. Both proteins had similar colocalized regions with LAMP2, but the RGR-d showed more colocalization with Rab7 (Fig. 2E).

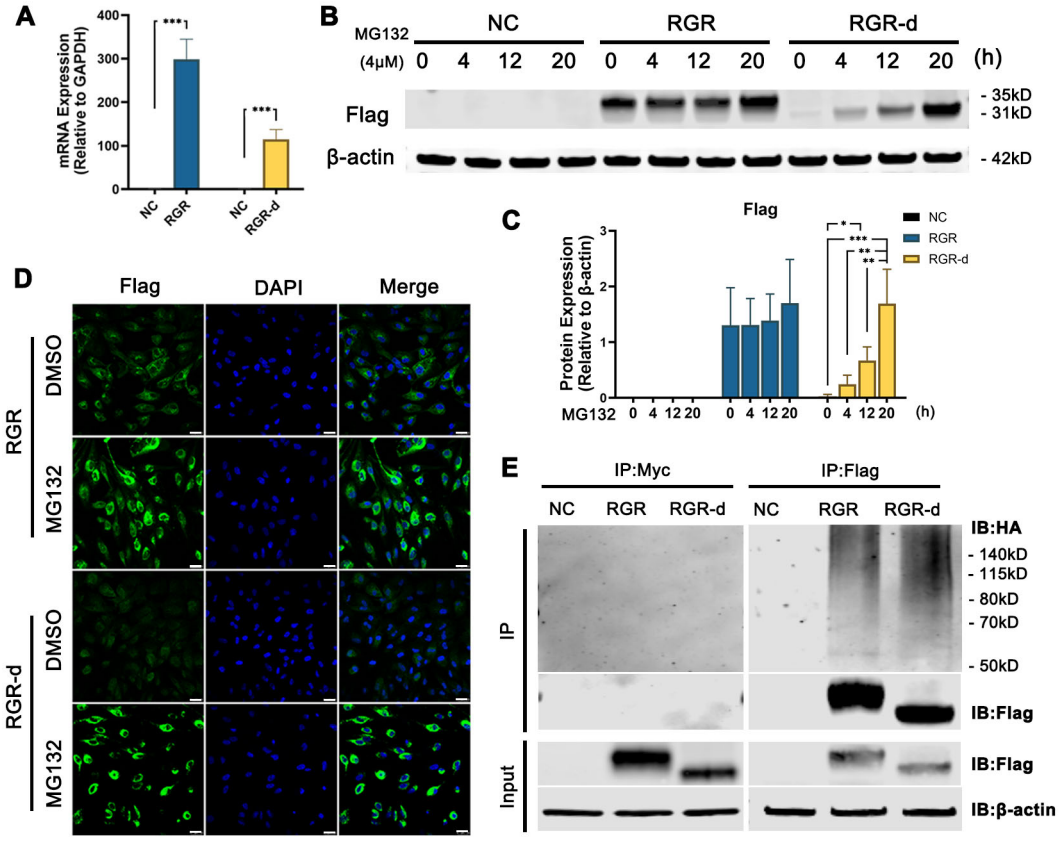

Figure 1. Degradation of RGR-d protein by the ubiquitin-proteasome system. ARPE-19 cells were stably transfected by NC-, RGR-, or RGR-d–overexpressing lentivirus, referred to as NC, RGR, and RGR-d cells. (**A**) Quantitative PCR detected significantly increased expression mRNA levels of the *RGR* and *RGR-d* gene in the corresponding transfected ARPE-19 cells. (**B**) Western blotting detected Flag-tagged RGR and RGR-d protein levels under treatment of 4 µM MG132, a 26S proteasome inhibitor. β-Actin levels serve as a protein loading control. (**C**) Quantification of Western blotting results in **B**. (**D**) Immunofluorescence assay showing expression of RGR and RGR-d. RGR-d protein could only be detected in the presence of MG132. *Scale bars*: 25 µm. (**E**) Co-IP using precoated Flag-beads demonstrated the level of polyubiquitin chains on RGR-d and RGR protein using the anti-HA antibody. The Myc-beads served as a negative control to exclude nonspecific binding by the Flag-beads. β-Actin levels serve as a protein loading control for input whole-cell lysates. Values in **A** and **C** are the mean ± SD. Statistics: unpaired two-tailed *t*-test (**A**), one-way ANOVA followed by Fisher's least significant difference (LSD) post hoc test (**C**). $^{*}P < 0.05$, $^{**}P < 0.01$, $^{***}P < 0.001$.

Investigative Ophthalmology & Visual Science

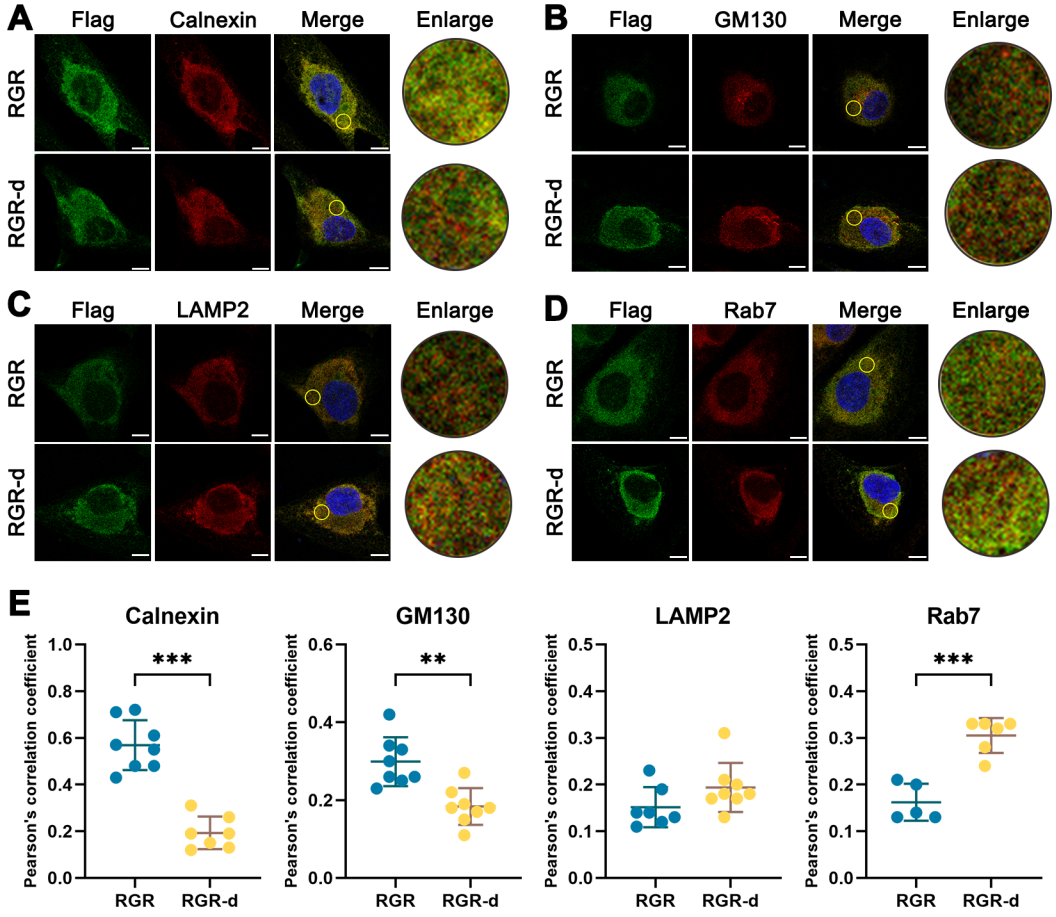

Figure 2. Mislocalization of RGR-d protein. The stably transfected RGR and RGR-d cells were treated with 2 µM MG132 for 16 hours. (**A–D**) Representative results of immunofluorescence double-labeling of Flag-tagged RGR or RGR-d with organelle markers: (**A**) ER marker, calnexin; (**B**) Golgi apparatus marker, GM130; (**C**) lysosome marker, LAMP2; and (**D**) marker for autophagosome and lysosome fusion, RAB7. (**E**) Quantitative analysis of Pearson's correlation coefficient, mean ± SD. *Scale bars*: (**A–D**) 10 µm. $^{*}P < 0.05$, $^{**}P < 0.01$, $^{***}P < 0.001$.

Under treatment of 4 µM MG132, all of the cells showed time-dependently increased autophagic flux, with the ratio of LC3bII/I reaching the peak at 12 hours and declining by 20 hours (Figs. 3A–C), and the RGR cells showed the maximum elevation. In the presence of BafA1, a late-stage autophagy inhibitor via blocking autophagosome–lysosome fusion,[26] the autophagic flux dramatically increased in all of the cells (Figs. 3D, 3F–G). Interestingly, regardless of the presence of MG132, the BafA1 treatment significantly increased the expression level of RGR, but such changes did not exist in RGR-d cells (Fig. 3E).

Enhanced ER Stress Due to RGR-d Accumulation

Cells were treated with MG132 in the presence or absence of TM, an ER stress inducer. There was no obvious difference in calnexin expression among all groups; however, a pronounced elevation of glucose regulated protein 78 (GRP78) was observed in RGR-d cells treated with DMSO or MG132 alone (Figs. 4A–C). Distinct regulation of the UPR pathways by RGR and RGR-d was reflected by expression profiles of the three signaling arms: inositol-requiring protein 1α (IRE1α), activating transcription factor 6 (ATF6), and protein kinase R-like endoplasmic reticulum kinase (PERK) (Figs. 4A, 4D–H). Compared to DMSO-treated RGR cells, RGR-d cells expressed significantly more PERK, CCAAT-enhancer-binding protein homologous protein (CHOP), and phosphorylated of IREα. The changes in RGR-d cells amplified in the presence of MG132. When TM was added, there was further enhanced phosphorylation of IREα and elevated expression of PERK and CHOP.

Further, we detected more early apoptotic cells (Figs. 4I–J, Supplementary Fig. S1A), lower cell portions of the S phase, higher percentages of the G0 to G1 phase (Figs. 4K–L, Supplementary Fig. S1B), and significantly less EdU-positive cells (Figs. 4M, 4N, Supplementary Fig. S1C) in MG132-treated RGR-d cells compared with the other two cell lines, reflecting the onset of the toxic effects of RGR-d protein accumulation. After added TM stimulation, the RGR-d cells showed significantly higher cell portions of late and early apoptosis, G0 to G1 arrest, and dramatically slowing cell proliferation, indicating severe cell damage under ER stress.

Cell Injury Induced by RGR-d Protein

We conducted a growth curve and found that RGR-d cells exhibited a slightly reduced proliferation rate in the absence of MG132, as the cell doubling time of negative control (NC), RGR, and RGR-d cells was 2 to 3 days, 3 to 4 days, and 5 to 6 days, respectively (Fig. 5A). This was consistent with the results of the EdU proliferation assay (Figs. 4M, 4N, Supplementary Fig. S1C), which demonstrated slowed cell proliferation of RGR-d cells even under DMSO-only

Investigative Ophthalmology & Visual Science

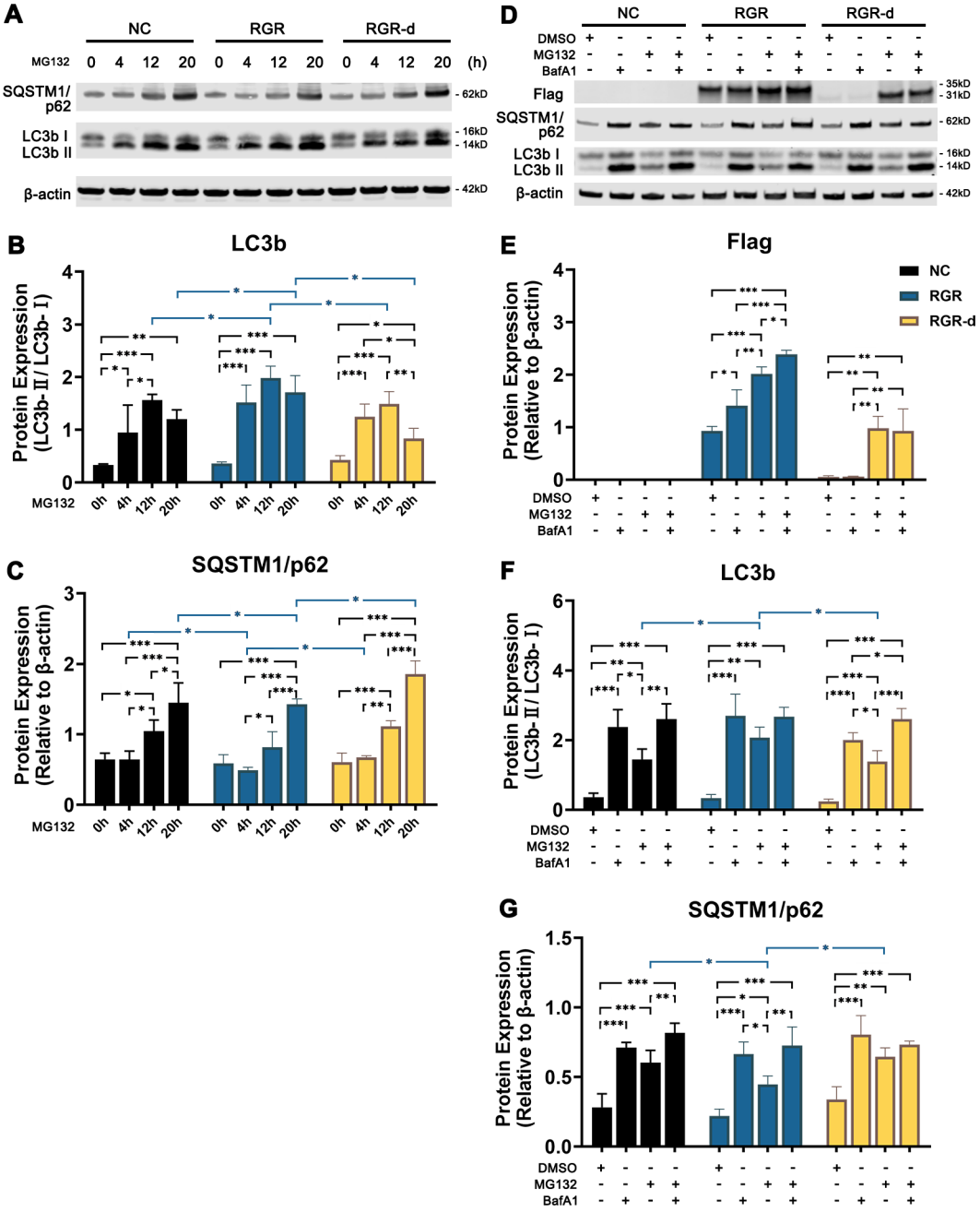

Figure 3. Lower activation of the autophagy–lysosomal pathway in RGR-d cells with impaired proteasome function. (**A**) The stably transfected NC, RGR, and RGR-d cells were treated with 4 µM MG132 for different durations. The expression of SQSTM1/p62 and LC3b was detected by Western blotting. (**B**, **C**) Quantification of Western blotting results in **A**. (**D**) The cells were treated with 4 µM MG132 combined with or without 50 nM bafilomycin A1 (BafA1) for 12 hours. The expression of SQSTM1/p62, LC3b, and Flag-tagged RGR and RGR-d was detected by Western blotting. (**E–G**) Quantification of Western blotting results in **D**. β-Actin levels serve as a protein loading control. Values in **B–C** and **E–G** are the mean ± SD. Statistics: one-way ANOVA followed by Fisher's LSD post hoc test (**B–C**, **E–G**). $^{*}P < 0.05$, $^{**}P < 0.01$, $^{***}P < 0.001$.

treatment. Upon treatment with 2 µM MG132, all of the cells exhibited spindle-shaped morphology, while the RGR-d cells demonstrated extensive cell death (Fig. 5B). CCK-8 assay results showed similar cell viability for the three groups under normal condition. Significant impairment of RGR-d cell viability initiated at the lowest concentration of MG132, and this sharp impairment was consistently maintained throughout increasing MG132 concentration. In contrast, the viability of NC and RGR cells showed a gradual inverse concentration dependence on MG132 (Fig. 5C).

We further explored the consequences of RGR-d accumulation in vivo since we previously detected fundus deposition of RGR-d in old RGR-d mice.[22] Zonula occludens 1 (ZO-1) labeling delineated tight junctions formed by RPE cells in 23-month-old WT mice, indicating intact barrier function. In contrast, in RGR-d mice at the same age, there was a remarkable disruption in ZO-1 expression, reflecting heavily impaired cell integrity of the RPE sheet possibly due to RGR-d deposition (Fig. 5D). Representative TUNEL assay images demonstrated that more photoreceptor

Investigative Ophthalmology & Visual Science

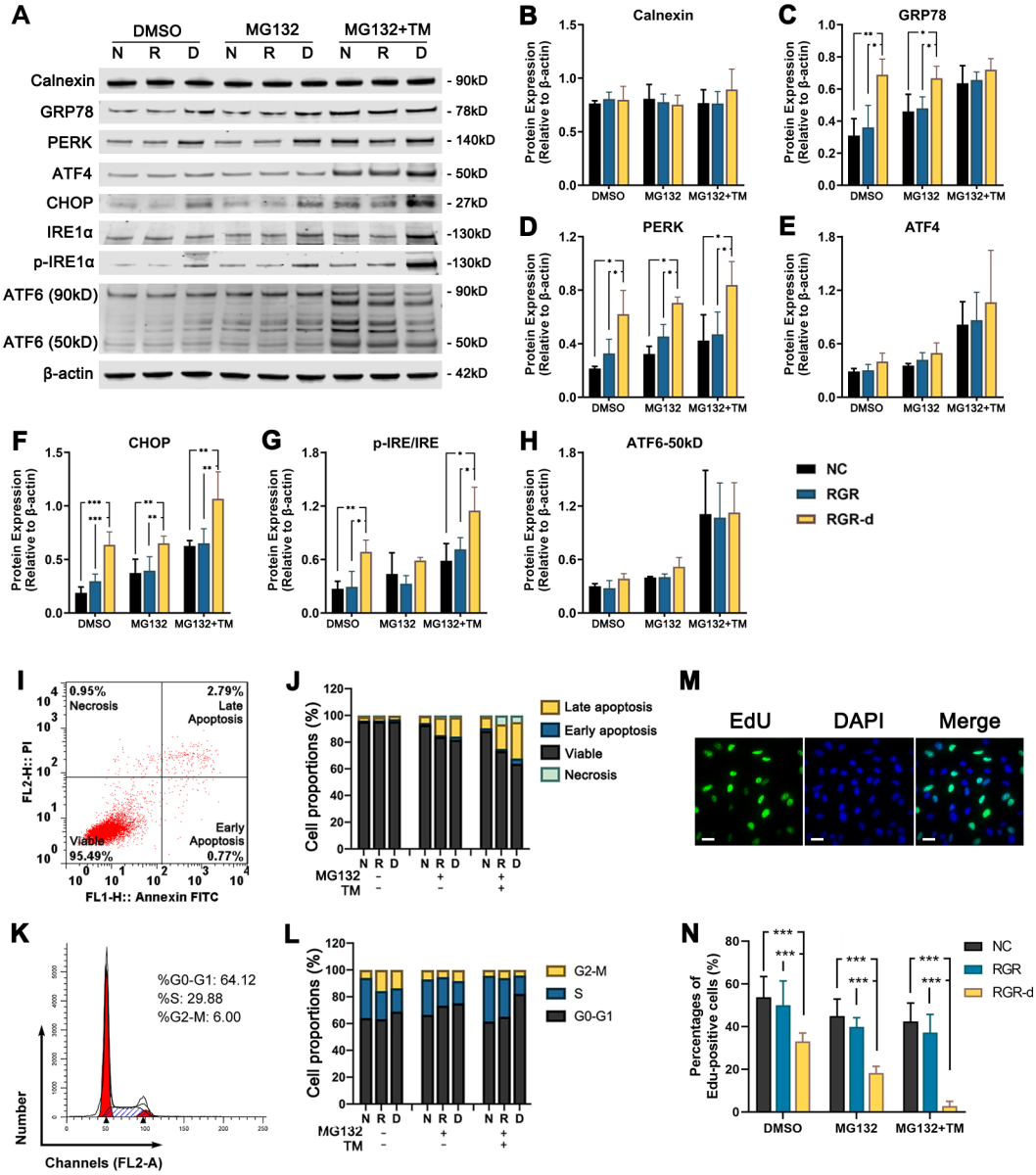

Figure 4. Aggravated ER stress in RGR-d cells. The stably transfected NC, RGR, and RGR-d cells were treated with 2 µM MG132 combined with or without 5 µg/mL TM for 16 hours. (**A**) The protein expression profile of ER stress and UPR pathways was analyzed by Western blotting. β-Actin levels serve as a protein loading control. (**B–H**) Quantification of the results in **A**, mean ± SD. (**I**, **J**) Representative result of cell apoptosis (DMSO-treated NC cells) determined by Annexin V-FITC/PI staining (**I**) and quantification data for all groups (**J**). (**K**, **L**) Representative result of cell cycle (DMSO-treated NC cells) determined by flow cytometry (**K**) and quantification data for all groups (**L**). (**M**, **N**) Representative result of the EdU assay for cell proliferation detection (DMSO-treated NC cells) (**M**) and quantification data for all groups (**N**), mean ± SD. *Scale bars*: (**M**) 250 µm. Statistics: one-way ANOVA followed by Fisher's LSD post hoc test (**B–H, N**). *$P < 0.05$, **$P < 0.01$, ***$P < 0.001$. D, RGR-d; N, negative control; R, RGR; TM, tunicamycin.

apoptosis occurred in 23-month-old RGR-d mice than in WT mice in the outer nuclear layer (Fig. 5E), especially in peripheral regions. These results suggested that RGR-d deposition could lead to significant RPE and photoreceptor dysfunction in aged RGR-d mice.

Complement C3 Deposition and Enhanced Inflammation in Aged RGR-d Mice

Our previous investigations used human donor eye tissue to reveal a potential involvement of the complement system in retinal damage related to RGR-d.[27] To further elaborate this relationship, we performed an immunofluorescence assay and found more deposition of the complement component C3 within the choriocapillaris of 23-month-old RGR-d mice compared to WT mice at the same age (Fig. 6A). Higher magnification merge of bright-field and fluorescent images indicated increased C3 deposition as RGR-d mice aged (Fig. 6B).

The retina and RPE–choroid of WT and RGR-d mice, which were 17 months old, were subjected to flow cytometry to investigate the recruitment and polarization of mononuclear phagocytes (Figs. 6C–I). The results detected a massive

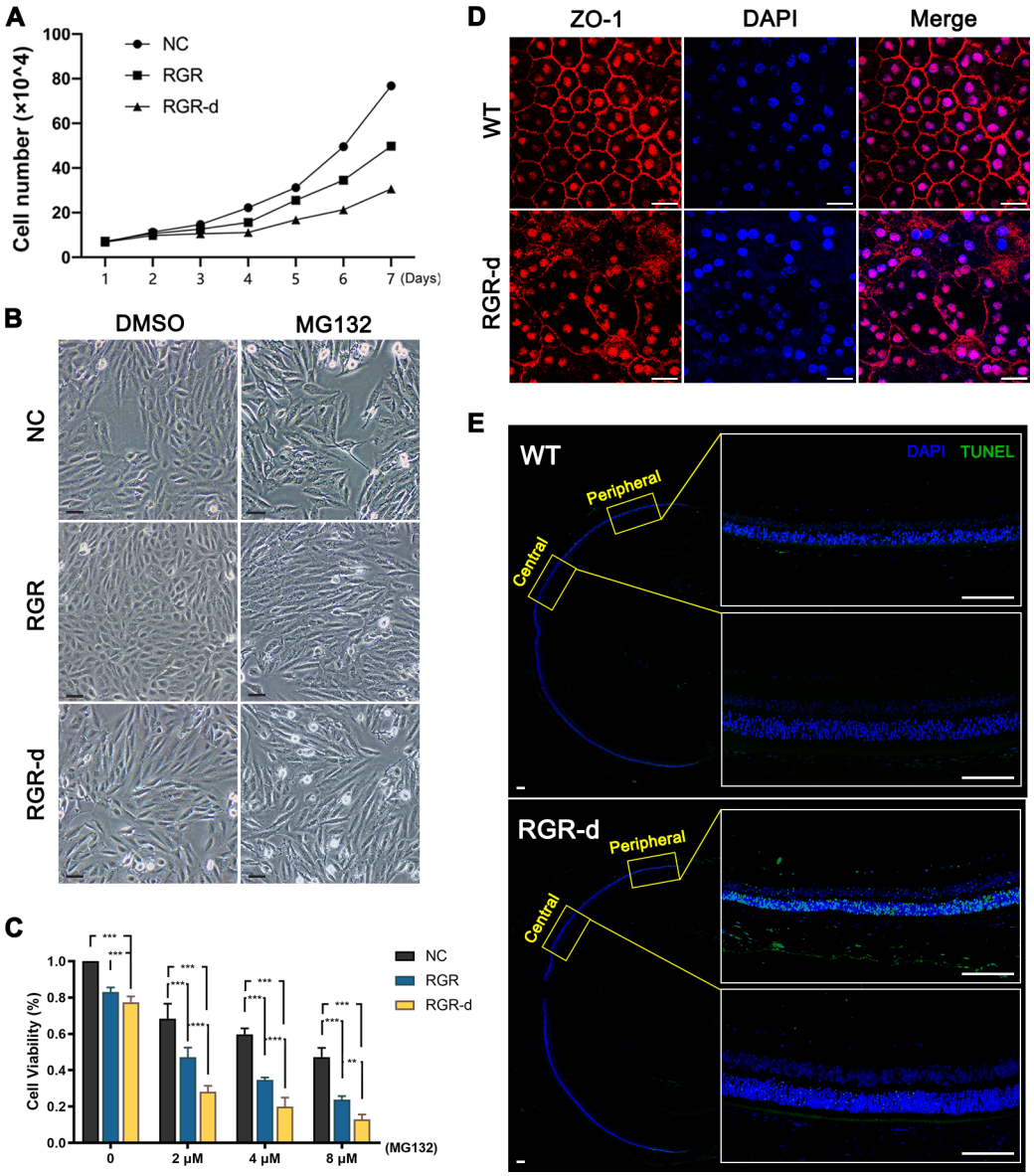

Figure 5. In vitro and in vivo analyses of cytotoxicity caused by RGR-d accumulation. Cytotoxicity caused by RGR-d accumulation. ARPE-19 cells were transfected by NC-, RGR-, or RGR-d–overexpressing lentivirus. (**A**) Growth curve showed that the proliferation of RGR-d cells slightly slowed down under normal culture. (**B**) After treatment of 2 μM MG132, the RGR-d cells exhibited the most severe cell morphology changes. (**C**) Cell viability assay by CCK-8 analysis showed the most extensive impaired cell viability of RGR-d cells when treated with different concentrations of MG132. Values are described as percentages to DMSO-treated NC cells, mean ± SD. (**D**) ZO-1 images show severely damaged RPE integrity in RGR-d mice compared with wild-type mice at 23 months old. (**E**) TUNEL assay of fundus sections showing the photoreceptor apoptotic level in peripheral and central fundus regions of RGR-d mice aged 23 months. *Scale bars*: 200 μm (**B**), 20 μm (**D**), and 100 μm (**E**). *$P < 0.05$, **$P < 0.01$, ***$P < 0.001$.

recruitment of peripheral macrophages ($CD11b^{+}CD45^{high}$) toward both the retina and RPE–choroid in RGR-d mice. In the RGR-d retina, the population of local microglia ($CD11b^{+}CD45^{low}$) showed a relative reduction, contrary to that in RPE–choroid (Figs. 6D, 6E). The proinflammatory cells ($CD86^{+}CD32^{+}$) (Figs. 6F, 6G) increased significantly with a concomitant reduction of anti-inflammatory cells ($CD163^{+}CD206^{+}$) (Figs. 6H, 6I) in both the retina and RPE–choroid of RGR-d mice. Moreover, GFAP, the marker of activation of Müller glia and gliosis, could be detected in RGR-d mice throughout the age range of 8 to 23 months (Supplementary Fig. S2). These results suggested a significant proinflammatory status of retina and RPE–choroid induced by RGR-d accumulation in aged mice.

Aggravated Damages in RGR-d Mice With High-Fat Diet

We provided RGR-d and WT mice of different ages with the Western diet as HFD and AIN-93M as the standard diet. The OCT and fundus photography demonstrated similar manifestations for RGR-d and WT mice at baseline (8 months old) (Fig. 7). After 3 months on HFD, WT mice showed drusen-like changes and slight fundus arteriosclerosis, in

Investigative Ophthalmology & Visual Science

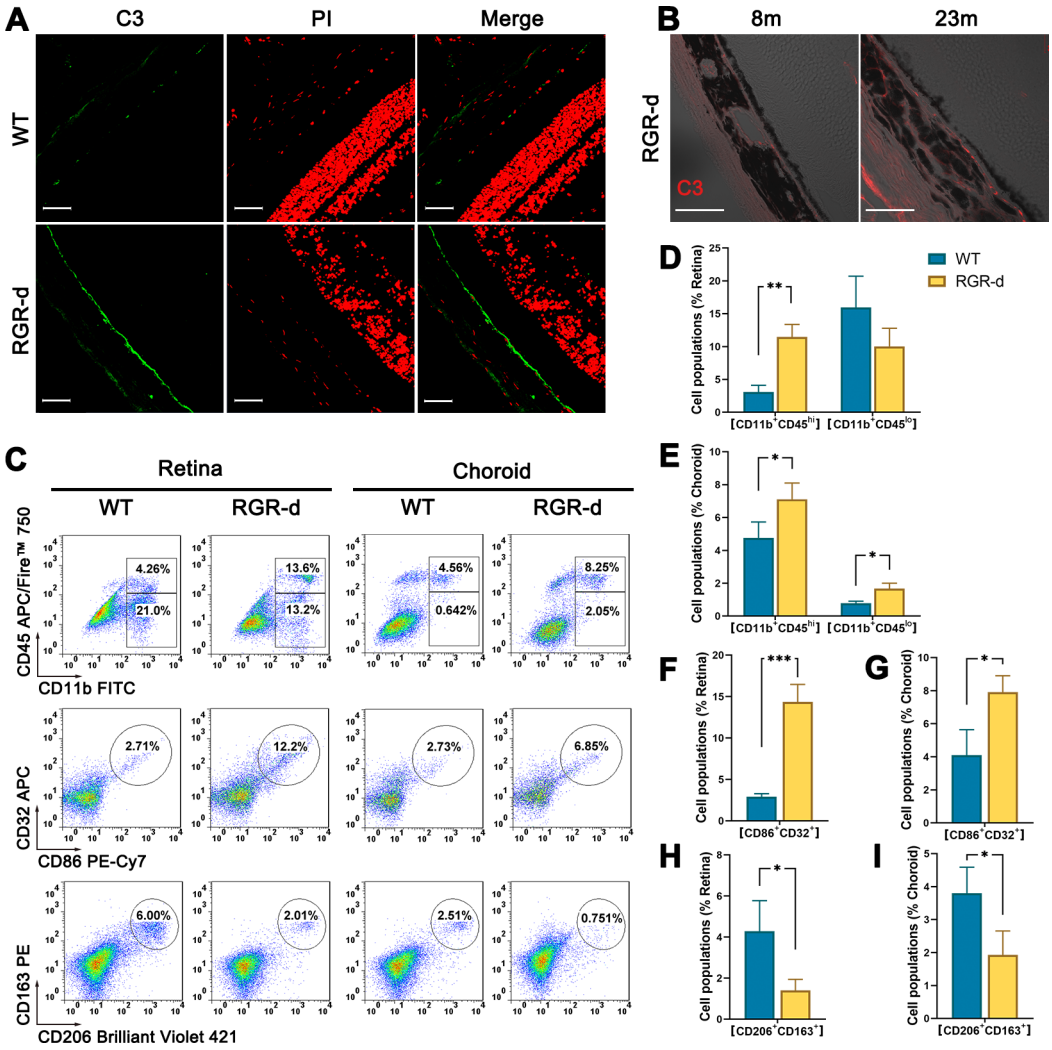

Figure 6. The proinflammatory tendency in retina and choroid of old RGR-d mice. (**A**) Immunofluorescence assay detected the existence of complement component C3 in the fundus of RGR-d mice aged 23 months. (**B**) Immunofluorescence signal of C3 merged with bright-field images detected increased C3 deposition within the choriocapillaris as RGR-d mice aged. (**C**) The retinas and RPE–choroids of WT and RGR-d mice were subjected to flow cytometry to determine the recruitment and polarization of mononuclear phagocytes, and the cell populations were further quantified in **D–I**. Increased peripheral macrophages ($CD11b^{+}CD45^{high}$), while reducing resident microglia ($CD11b^{+}CD45^{low}$), were detected in retinas (**D**) of RGR-d mice. $CD11b^{+}CD45^{high}$ peripheral macrophages were recruited, and $CD11b^{+}CD45^{low}$ resident microglia migrated toward RPE–choroids in RGR-d mice (**E**). RGR-d mice showed a significantly increased proportion of $CD86^{+}CD32^{+}$ proinflammatory cells in retinas (**F**) and RPE–choroids (**G**), as long as there was a reduction of $CD163^{+}CD206^{+}$ anti-inflammatory population in retinas (**H**) and RPE–choroids (**I**). *Scale bars*: 50 µm (**A**, **B**). Values in **D–I** are described as mean ± SD. Statistics: unpaired two-tailed *t*-test (**D–I**). $^{*}P < 0.05$, $^{**}P < 0.01$, $^{***}P < 0.001$.

comparison to AIN-fed mice. Both AIN- and HFD-fed RGR-d mice manifested severe pigmental atrophy and arteriosclerosis, with the HFD group being more significant. It worth mentioning that nearly all of the old RGR-d mice developed opaque cataracts, causing most fundus regions of RGR-d mice invisible via OCT or fundus photography. While within the detectable area, the HFD-fed RGR-d mice showed the most serious drusen-like lesions, patchy depigmentation, and RPE continuity interruptions (Fig. 7).

The results of HE staining of 11-month-old RGR-d mice demonstrated more disorganized arrangement, a thinner outer nuclear layer, fewer photoreceptors, an enlarged intercellular space, and greater RPE depigmentation and discontinuity compared to WT mice of the same age and diet (Fig. 8A). In addition, RGR-d mice developed a distinct eosinophilic sub-RPE layer that appeared thicker in the HFD-fed animals. These changes were more pronounced in the 17-month-old RGR-d mice, who started a high-fat or maintained a standard diet at 14 months, and the older RGR-d mice with HFD showed the worst histologic injuries among all of the groups (Fig. 8A). In addition, there was apparent capillary atrophy in RGR-d mice at 17 months old, as even sclerotic extracellular tissue could be observed in close proximity to Bruch's membrane in HFD-fed RGR-d mice (Fig. 8B). Among the mice fed with standard diet, outer nuclear layer (ONL) thickness was thinner in 17-month-old RGR-d mice compared to 17-month-old WT mice. ONL thinning could also be observed in HFD-fed RGR-d mice in both central and peripheral regions compared with HFD-fed WT mice at an even earlier age of 11 months. Older RGR-d mice were more susceptible to HFD, since significantly thinner ONL, photoreceptor layer, and inner nuclear layer of peripheral retina were observed, compared to that of older WT mice (Fig. 8C).

Investigative Ophthalmology & Visual Science

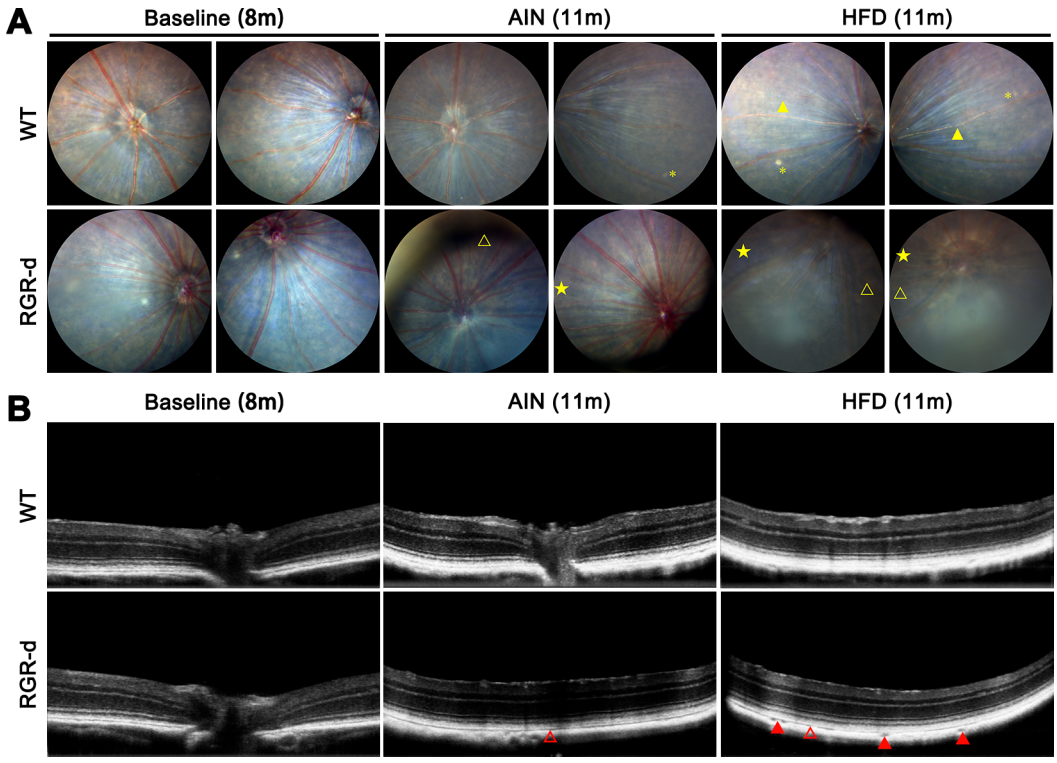

Figure 7. OCT and fundus photography manifestations of WT and RGR-d mice fed with standard AIN diet or HFD. (**A**) Representative fundus photography. At 11 months (AIN-fed), WT mice showed subtle drusen-like deposits (*yellow asterisk*), and RGR-d mice showed depigmentation (*yellow star*) and thinning and stiffening of artery vessels (*blank yellow triangle*). HFD promoted fundus impairment, as the HFD-fed WT mice showed enhanced arterial reflection (*solid yellow triangle*) in addition. HFD-fed RGR-d mice showed the worst pathologic changes and severe refractive media opacity. (**B**) Representative OCT images. At 11 months, AIN- and HFD-fed RGR-d mice showed developed RPE discontinuity (*blank red triangle*), and sub-RPE hyporeflections (*solid red triangles*) could be observed in HFD-fed RGR-d mice.

Abnormalities and degeneration of the RPE and Bruch's membrane in HFD-fed RGR-d mice were further analyzed by transmission electron microscopy after 3 months of the corresponding diet (Fig. 9). There was no obvious Bruch's membrane disruption or sub-RPE deposit formation in the 11-month-old AIN-fed WT mice or HFD-fed WT mice. Bruch's membrane was slightly thicker in AIN-fed RGR-d mice than in AIN-fed WT mice of the same age. Notably, 11-month-old HFD-fed RGR-d mice showed greater thickness and higher heterogeneity of Bruch's membrane, charcoal-like pigments in the RPE, and notable drusen-like metabolites at the basal side of the RPE. For older WT mice, although there were no obvious sub-RPE deposits, Bruch's membrane thickness and heterogeneity seemed to increase in 17-month-old HFD-fed mice when compared to either AIN-fed WT mice of the same age or the HFD-fed younger WT mice (11 months old). When it came to 17-month-old RGR-d mice, AIN-fed mice showed slight increases in Bruch's membrane thickness and heterogeneity, but these changes were markedly greater in the HFD-fed RGR-d mice at the same age who also exhibited abundant drusen-like deposits in the sub-RPE space. Both AIN- and HFD-fed RGR-d mice at an older age showed narrowed capillary lumen, indicating choriocapillaris atrophy.

Discussion

The UPS and the autophagy-lysosomal pathway (ALP) are the two major protein degradation pathways that evolved in eukaryotic cells. Protein dyshomeostasis in RPE cells and subsequent deposits of abnormal metabolites have been considered among the main causes of drusen formation in AMD pathogenesis.[28,29] Our study emphasized an abnormal protein with altered conformation—namely, RGR-d, whose accumulation may cause severe cell damage and result in drusen-like deposits and retina–choriocapillaris inflammation and atrophy.

Traditionally, the UPS and ALP were thought to act separately: most newly synthesized or short-lived proteins are ubiquitinated and degraded via the UPS; most long-lived proteins, such as organelle-associated proteins and membrane-encapsulated proteins, go through the ALP pathway and are hydrolyzed. More recently, a growing body of literature suggests that the two pathways can work synergistically and even in direct communication under certain conditions.[30–32] In this study, we found that the RGR-d protein was almost completely cleared in ARPE-19 cells under conventional cultivation but was found in abundance and highly ubiquitinated in the presence of MG132. This behavior suggests that UPS is the primary route by which RGR-d may undergo degradation.

Under treatment with MG132, RGR-d showed greater colocalization with Rab7 compared to RGR. Regardless of MG132 treatment, the expression of RGR remarkedly increased in the presence of BafA1, but there was no such change in RGR-d expression. Notably, RGR exhibited the greatest magnitude of change in autophagy activation, while the RGR-d and NC cells were almost equivalent. This evidence revealed an alternative degradation pattern for RGR by ALP but not for the abnormal RGR-d. Thus,

Investigative Ophthalmology & Visual Science

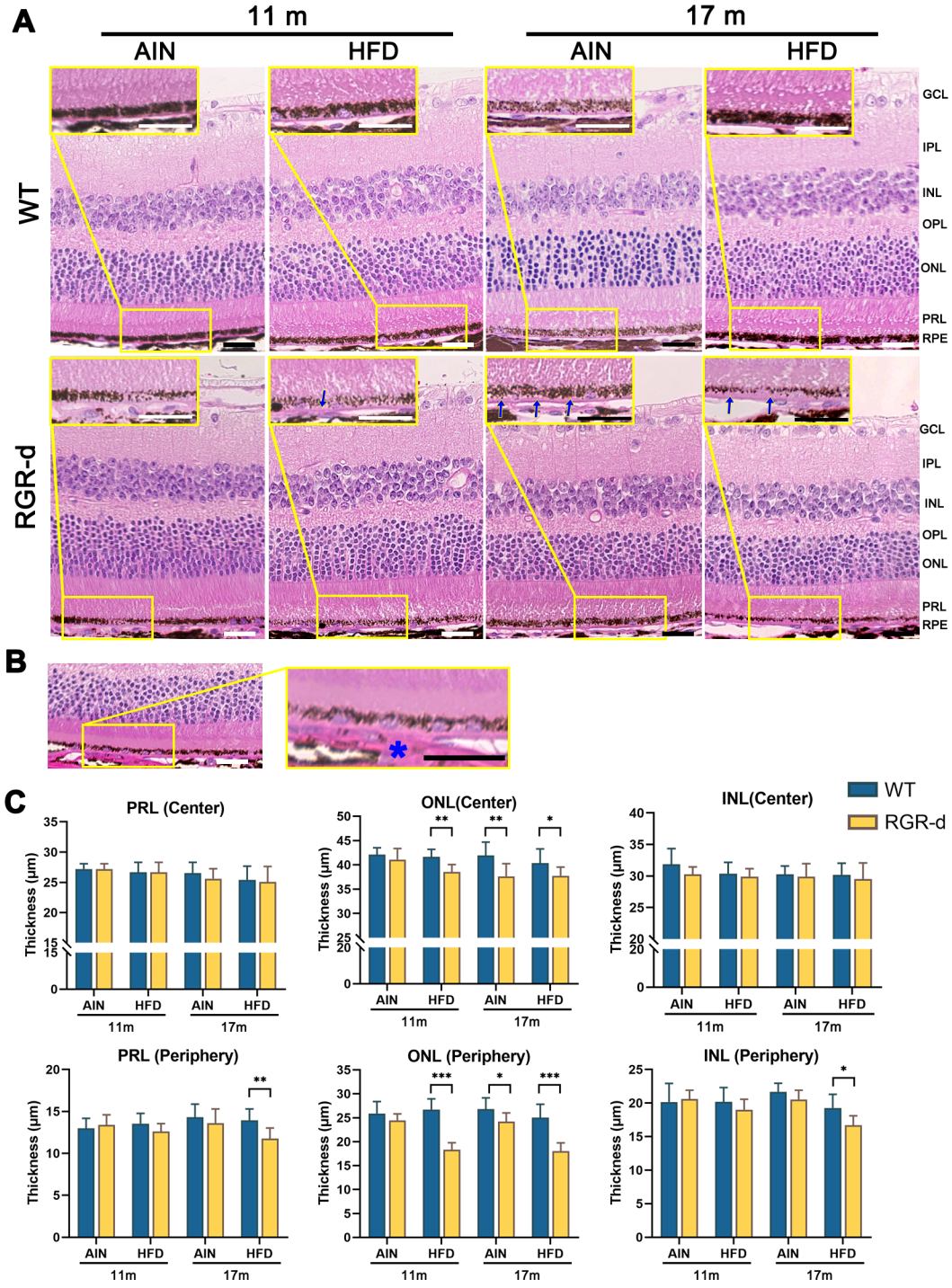

Figure 8. HE staining of WT and RGR-d mice at 11 or 17 months old fed with a standard AIN-93M or HFD. (**A**) Disorganized arrangement, thinner ONL, fewer photoreceptors, and RPE depigmentation and discontinuity in older and HFD-fed RGR-d mice, who furthermore developed a distinctive eosinophilic sub-RPE layer (*blue arrows*). The HFD-fed RGR-d mice exhibited the worst histologic injuries among all groups. (**B**) The 17-month-old RGR-d mice with the HFD showed the most severe choriocapillaris atrophy, as the *blue asterisk* shows the presence sclerotic extracellular tissue adjacent to Bruch's membrane. (**C**) Quantitative thickness of PRL, ONL, and INL; values are the mean ± SD. **Scale bars**: (**A**) 25 μm. GCL, ganglion cell layer; INL, inner nuclear layer; IPL, inner plexiform layer; OPL, outer plexiform layer; PRL, photoreceptor layer. *$P < 0.05$, **$P < 0.01$, ***$P < 0.001$.

when the proteasome is impaired, both RGR and RGR-d accumulate, and autophagy more strongly acts on the RGR protein rather than on RGR-d, leading to a successful degradation of normal RGR but intracellular retention of abnormal RGR-d. The final fate of RGR-d protein still requires further investigation. Moreover, as reported previously, an active autophagic pathway was protective after MG132 treatment, and ALP can partially compensate for an impaired proteasome.[33] Thus, the relatively lower increase of autophagic flux might indicate a diminished capability of self-compensation

Investigative Ophthalmology & Visual Science

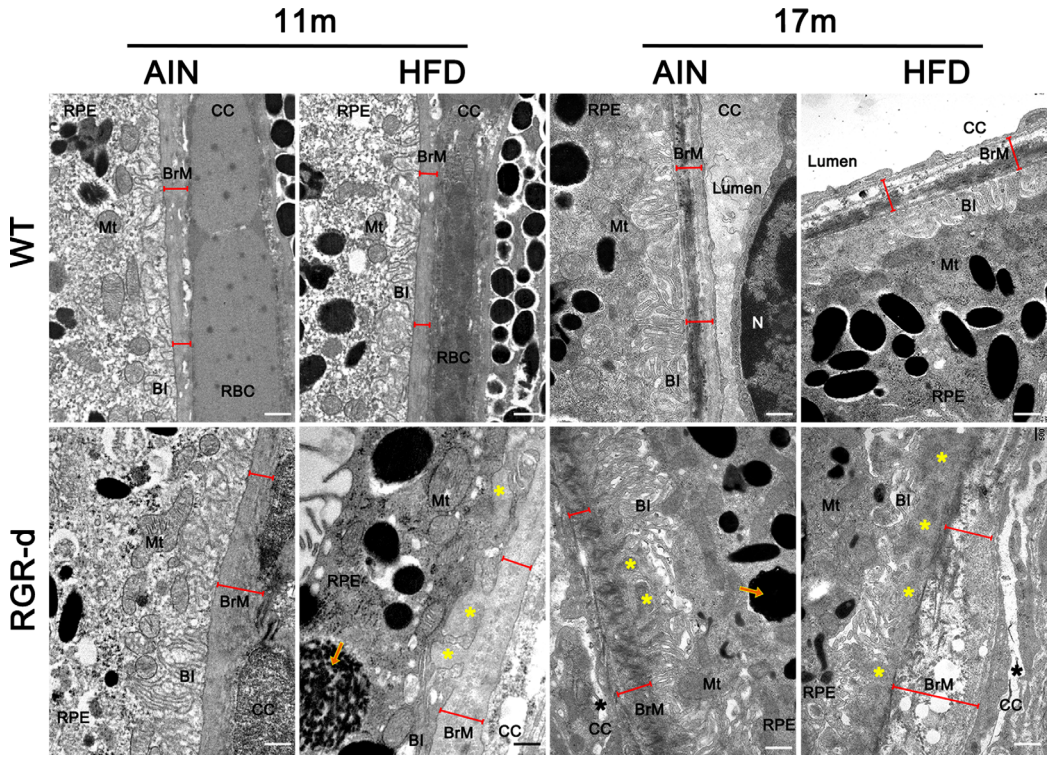

Figure 9. The transmission electron microscopy images showed increased thickness and heterogeneity of Bruch's membrane (*red line segments*) in RGR-d mice, especially in 17-month-old HFD-fed mice. The 11-month-old RGR-d mice fed with the HFD showed charcoal-like pigments (*orange arrows*) and notable drusen-like metabolites (*yellow asterisks*) excreted from the basal side of the RPE. Narrowed choriocapillaris lumen (*black asterisks*) could be observed in 17-month-old RGR-d mice, and those fed with the HFD showed the most significant pathologic changes. BI, basal infoldings; BrM, Bruch's membrane; CC, choriocapillaris; Mt, mitochondria; N, nucleus; RBC, red blood cell. *Scale bars*: 500 nm.

and self-protection of RGR-d cells to some extent. Our results highlighted the major point that normal RGR and abnormal RGR-d had quite different processing patterns.

It is reported that proteins produced by translation of mutated or abnormal transcripts are substantially more likely to misfold than wild-type proteins.[34–36] Compared to RGR-d, RGR showed much better colocalization with the ER and Golgi apparatus. This illustrated mislocalization of the RGR-d likely due to aberrant protein folding in the ER or further modification in the Golgi apparatus of the abnormal RGR-d protein. GRP78, an important ER stress chaperone molecule, regulates the UPR sensors and downstream pathways. That is, upregulated GRP78 suggests a severe protein misfolding condition.[37,38] Our study demonstrated higher levels of GRP78 in untreated RGR-d cells, implying a potential upregulation of chaperone molecules despite virtually complete RGR-d elimination. MG132 treatment resulted in significantly faster deterioration of RGR-d cell viability despite further increased GRP78 level, suggesting that elevated chaperones are still incapable of assisting correct folding of RGR-d or relieving cell damages.

Proteostasis perturbation elicits ER stress and triggers UPR via IRE1α, ATF6, or PERK, in order to mitigate the injury led by misfolded proteins.[39,40] Mild ER stress tends to promote the activation of genes involved in damage control, whereas sustained or severe ER stress is attributed to the activation of prodeath genes.[41] We detected elevated PERK, CHOP, and IRE1α along with increased IRE1α phosphorylation in RGR-d cells with no MG132 or TM, indicating that UPR had been provoked at baseline, independent of intracellular RGR-d accumulation. These changes were maintained or amplified when the cells were treated with MG132, either with or without TM, implicating perpetual ER stress and highly activated UPR in RGR-d cells. Moreover, when RGR-d first began to accumulate in the presence of MG132, the UPR was initiated, but the cells were still in their adaptive phase, where prosurvival genes like GRP78 were elevated, with no obvious increase in the proportion of apoptotic cells. When TM elicited ER stress in all the cells, the NC and RGR cells entered the adaptive phase; however, the RGR-d cells appeared to develop into the decompensation phase, as shown by further elevation of proapoptotic CHOP and the much more extensive apoptosis proportion. Taken together, ER stress should be highlighted as the critical mechanism underlying RGR-d–induced injury.

The damages caused by RGR-d deposition were further elucidated by in vitro and in vivo experiments. The cell proliferation and viability assays showed a decrease in RGR-d cell functions in the absence of MG132, but severe deterioration occurred upon the presence of MG132. It is worth mentioning that the cell apoptosis assay (Fig. 4J) did not show a significant difference between RGR and RGR-d upon MG132 treatment, while in contrast, a significant difference in cell viability (Fig. 5C) and proliferation (Fig. 4N) was observed between these groups. This inconsistency was reasonable because the cell viability assay detected the number of tested cells normalized to that of NC cells in the absence of MG132, while the apoptosis assay measured the distribution of stages of apoptosis among the reduced pool of viable cells that remained under each condition.

Investigative Ophthalmology & Visual Science

In normal culture medium, RGR-d cells (and RGR cells, to a lesser degree) grow slower than the control cells. This slow growth defect may be due to a wasting of cellular energy and resources on continuous processing of misfolded RGR-d, rather than apoptosis per se. Under MG132-induced stress, RGR-d cells grow even slower with the emergence of elevated ER stress and apoptosis. The cell viability result is variant because of at least two different reasons for slower cell growth, as it factors in both apoptosis and the wasting of cellular energy and resources.

The RPE of 17-month-old RGR-d mice exhibited irregular shape and size with poor demarcation of ZO-1 labeling, as well as significantly increased apoptosis in the ONL of aged RGR-d mice. These results intuitively demonstrated impaired barrier function of the RPE layer and increased photoreceptor death caused by RGR-d deposition.

Local chronic inflammation caused by activated microglia recruitment to the deposit site and subsequent upregulation of the complement system is believed to contribute to drusen formation.[42,43] We previously reported that the spatial distribution of complement factor C5b-9 closely matched the presence of RGR-d in a 78-year-old male donor eye tissue,[27] consistent with the current study demonstrating strong and linear distribution of complement component C3 in the choriocapillaris of older RGR-d mice. Inflammation responses were significantly enhanced in the retina and RPE–choroid of RGR-d mice, revealed by the recruitment of peripheral monocytes and their shift to a proinflammation direction. Furthermore, microglia resident in retina seemed to migrate to the RPE–choroid region, consistent with the condition of deposit formation in aged RGR-d mice.

Upregulated GFAP indicated activation and gliosis of Müller glia cells, consistent with the inflammatory status of the RGR-d retina. Nevertheless, the potential and interesting effects of RGR-d in Müller glia cells are not yet clarified in our mouse model. A possible mitigating factor is that RGR gene expression is markedly low in mouse Müller cells, relative to the expression in RPE. Perhaps more likely is that the processing behavior and trafficking of RGR-d may be quite different in Müller cells and less detrimental. Future studies would be geared to identifying key conditions and main intracellular factors that increase or decrease the proteotoxicity of mutant RGR-d.

Abundant data suggest that a high-fat diet, an independent risk of AMD,[44,45] could induce oxidative stress and inflammation[46] and is associated with impaired proteostasis[47] and aggravated ER stress.[48,49] Consistent with the RGR-d–related pathologic environment including disturbed proteostasis, ER stress, extensive cell dysfunction, and increased proinflammatory status, a high-fat diet (Western diet) accelerated and aggravated the pathologic changes in both 11- and 17-month-old RGR-d mice, especially in the peripheral fundus. Compared to the 11-month-old RGR-d mice, 17-month-old HFD-fed mice demonstrated the most severe pathologic manifestations, including RPE depigmentation, sub-RPE deposition, Bruch's membrane thickening, ONL thinning, and choroidal atrophy. These results may be interpreted as the weakened ability of cell self-clearance with aging that cannot counter the accumulation of misfolded RGR-d, hence predisposing the retina and RPE–choroid to a pathologic status. A high-fat diet perturbs metabolism and drives disease through multiple mechanisms, giving rise to persistent chronic inflammation[44,50] and disturbed proteostasis,[51] and it ultimately accelerates the development of drusen-like deposits and AMD-like phenotypes.

In the current study, we used WT mice instead of $RGR^{-/-}$ knockout mice as the control group. Since the ER stress, UPR, and cytotoxicity were first compared between RGR-d and RGR cell lines, it was appropriate to evaluate in a parallel manner phenotype differences between mice expressing RGR-d and RGR (i.e., WT mice). Mice that express even normal RGR were important to rule out any age-related, or stress-induced, deleterious effects of normal RGR, which may itself undergo significant protein degradation. The $RGR^{-/-}$ mice with loss of normal RGR appeared normal, since retinal degeneration has not been reported in $RGR^{-/-}$ mice.[52] Previously, we have used RGR-d with control $RGR^{-/-}$ knockout mice to analyze degeneration of the choriocapillaris, RPE, and photoreceptors.[22] Furthermore, the *RGR* gene is wholly lost in marsupials,[53] and this loss is likely tolerated.

In summary, the protein control system of RPE plays a critical role in maintaining protein homeostasis by intensive clearance of misfolded proteins such as RGR-d. Deterioration of cell clearance capacity under a pathologic environment, such as aging, would lead to the accumulation of abnormal proteins and perpetual ER stress, causing RPE injuries and sub-RPE deposits. Our study revealed the pathogenicity of an abnormal isoform of the *RGR* gene and addressed the significant role of proteopathy in AMD. These findings may contribute to greater comprehension of the multifactorial causes of AMD.

Acknowledgments

Supported by the National Natural Science Foundation of China (NSFC No. 82171060) and the National Key R&D Program of China (No. 2020YFC2008200).

This study was performed in line with the principles of the Declaration of Helsinki. Approval was granted by the Peking University People's Hospital institutional review board (Approval no. 2019PHC027).

Disclosure: **C. Ren**, None; **H. Cui**, None; **X. Bao**, None; **L. Huang**, None; **S. He**, None; **H.K.W. Fong**, None; **M. Zhao**, None

References

1. Keeling E, Culling AJ, Johnston DA, et al. An in-vitro cell model of intracellular protein aggregation provides insights into RPE stress associated with retinopathy. *Int J Mol Sci*. 2020;21(18):6647.
2. Hetz C, Saxena S. ER stress and the unfolded protein response in neurodegeneration. *Nat Rev Neurol*. 2017;13(8):477–491.
3. Balusu S, Praschberger R, Lauwers E, De Strooper B, Verstreken P. Neurodegeneration cell per cell. *Neuron*. 2023;111(6):767–786.
4. Green WR. Histopathology of age-related macular degeneration. *Mol Vis*. 1999;5:27.
5. Chirco KR, Sohn EH, Stone EM, Tucker BA, Mullins RF. Structural and molecular changes in the aging choroid: implications for age-related macular degeneration. *Eye (Lond)*. 2017;31(1):10–25.
6. Ferrington DA, Sinha D, Kaarniranta K. Defects in retinal pigment epithelial cell proteolysis and the pathology associated with age-related macular degeneration. *Prog Retin Eye Res*. 2016;51:69–89.

7. Aragonès G, Dasuri K, Olukorede O, et al. Autophagic receptor p62 protects against glycation-derived toxicity and enhances viability. *Aging Cell*. 2020;19(11):e13257.
8. Blasiak J, Pawlowska E, Szczepanska J, Kaarniranta K. Interplay between autophagy and the ubiquitin-proteasome system and its role in the pathogenesis of age-related macular degeneration. *Int J Mol Sci*. 2019;20(1):210.
9. Xu C, Bailly-Maitre B, Reed JC. Endoplasmic reticulum stress: cell life and death decisions. *J Clin Invest*. 2005;115(10):2656–2664.
10. Sitia R, Braakman I. Quality control in the endoplasmic reticulum protein factory. *Nature*. 2003;426(6968):891–894.
11. Pohl C, Dikic I. Cellular quality control by the ubiquitin-proteasome system and autophagy. *Science*. 2019;366(6467):818–822.
12. Flores-Bellver M, Mighty J, Aparicio-Domingo S, et al. Extracellular vesicles released by human retinal pigment epithelium mediate increased polarised secretion of drusen proteins in response to AMD stressors. *J Extracell Vesicles*. 2021;10(13):e12165.
13. Johnson LV, Forest DL, Banna CD, et al. Cell culture model that mimics drusen formation and triggers complement activation associated with age-related macular degeneration. *Proc Natl Acad Sci USA*. 2011;108(45):18277–18282.
14. Galloway CA, Dalvi S, Hung SSC, et al. Drusen in patient-derived hiPSC-RPE models of macular dystrophies. *Proc Natl Acad Sci USA*. 2017;114(39):E8214–E8223.
15. Usui H, Nishiwaki A, Landiev L, et al. In vitro drusen model—three-dimensional spheroid culture of retinal pigment epithelial cells. *J Cell Sci*. 2018;132(4):jcs215798.
16. Jiang M, Pandey S, Fong HK. An opsin homologue in the retina and pigment epithelium. *Invest Ophthalmol Vis Sci*. 1993;34(13):3669–3678.
17. Jiang M, Shen D, Tao L, et al. Alternative splicing in human retinal mRNA transcripts of an opsin-related protein. *Exp Eye Res*. 1995;60(4):401–406.
18. Fong HK, Lin MY, Pandey S. Exon-skipping variant of RGR opsin in human retina and pigment epithelium. *Exp Eye Res*. 2006;83(1):133–140.
19. Morshedian A, Kaylor JJ, Ng SY, et al. Light-driven regeneration of cone visual pigments through a mechanism involving RGR opsin in Müller glial cells. *Neuron*. 2019;102(6):1172–1183.e1175.
20. Choi EH, Daruwalla A, Suh S, Leinonen H, Palczewski K. Retinoids in the visual cycle: role of the retinal G protein-coupled receptor. *J Lipid Res*. 2021;62:100040.
21. Kiser PD, Palczewski K. Pathways and disease-causing alterations in visual chromophore production for vertebrate vision. *J Biol Chem*. 2021;296:100072.
22. Bao X, Zhang Z, Guo Y, et al. Human RGR gene and associated features of age-related macular degeneration in models of retina-choriocapillaris atrophy. *Am J Pathol*. 2021;191(8):1454–1473.
23. Lin MY, Kochounian H, Moore RE, et al. Deposition of exon-skipping splice isoform of human retinal G protein-coupled receptor from retinal pigment epithelium into Bruch's membrane. *Mol Vis*. 2007;13:1203–1214.
24. Li X, Li X, He S, Zhao M. MeCP2-421-mediated RPE epithelial-mesenchymal transition and its relevance to the pathogenesis of proliferative vitreoretinopathy. *J Cell Mol Med*. 2020;24(16):9420–9427.
25. Papaioannou VE, Fox JG. Efficacy of tribromoethanol anesthesia in mice. *Lab Anim Sci*. 1993;43(2):189–192.
26. Mauvezin C, Neufeld TP. Bafilomycin A1 disrupts autophagic flux by inhibiting both V-ATPase-dependent acidification and Ca-P60A/SERCA-dependent autophagosome-lysosome fusion. *Autophagy*. 2015;11(8):1437–1438.
27. Kochounian H, Zhang Z, Spee C, Hinton DR, Fong HK. Targeting of exon VI-skipping human RGR-opsin to the plasma membrane of pigment epithelium and co-localization with terminal complement complex C5b-9. *Mol Vis*. 2016;22:213–223.
28. Bilbao-Malavé V, González-Zamora J, de la Puente M, et al. Mitochondrial dysfunction and endoplasmic reticulum stress in age related macular degeneration, role in pathophysiology, and possible new therapeutic strategies. *Antioxidants (Basel)*. 2021;10(8):1170.
29. McLaughlin T, Medina A, Perkins J, et al. Cellular stress signaling and the unfolded protein response in retinal degeneration: mechanisms and therapeutic implications. *Mol Neurodegener*. 2022;17(1):25.
30. Pla-Prats C, Thomä NH. Quality control of protein complex assembly by the ubiquitin-proteasome system. *Trends Cell Biol*. 2022;32(8):696–706.
31. Dubnikov T, Ben-Gedalya T, Cohen E. Protein quality control in health and disease. *Cold Spring Harb Perspect Biol*. 2017;9(3):a023523.
32. Amm I, Sommer T, Wolf DH. Protein quality control and elimination of protein waste: the role of the ubiquitin-proteasome system. *Biochim Biophys Acta*. 2014;1843(1):182–196.
33. Kato M, Ospelt C, Gay RE, Gay S, Klein K. Dual role of autophagy in stress-induced cell death in rheumatoid arthritis synovial fibroblasts. *Arthritis Rheumatol*. 2014;66(1):40–48.
34. Wilson MR, Satapathy S, Jeong S, Fini ME. Clusterin, other extracellular chaperones, and eye disease. *Prog Retin Eye Res*. 2022;89:101032.
35. Kumar A, Biswas P. Effect of site-directed point mutations on protein misfolding: a simulation study. *Proteins*. 2019;87(9):760–773.
36. Nemtseva EV, Gerasimova MA, Melnik TN, Melnik BS. Experimental approach to study the effect of mutations on the protein folding pathway. *PLoS One*. 2019;14(1):e0210361.
37. Zhu G, Lee AS. Role of the unfolded protein response, GRP78 and GRP94 in organ homeostasis. *J Cell Physiol*. 2015;230(7):1413–1420.
38. Elfiky AA, Baghdady AM, Ali SA, Ahmed MI. GRP78 targeting: hitting two birds with a stone. *Life Sci*. 2020;260:118317.
39. Cybulsky AV. Endoplasmic reticulum stress, the unfolded protein response and autophagy in kidney diseases. *Nat Rev Nephrol*. 2017;13(11):681–696.
40. Hetz C. The unfolded protein response: controlling cell fate decisions under ER stress and beyond. *Nat Rev Mol Cell Biol*. 2012;13(2):89–102.
41. Tabas I, Ron D. Integrating the mechanisms of apoptosis induced by endoplasmic reticulum stress. *Nat Cell Biol*. 2011;13(3):184–190.
42. Kauppinen A, Paterno JJ, Blasiak J, Salminen A, Kaarniranta K. Inflammation and its role in age-related macular degeneration. *Cell Mol Life Sci*. 2016;73(9):1765–1786.
43. Liisborg C, Skov V, Kjær L, Hasselbalch HC, Sørensen TL. Patients with MPNs and retinal drusen show signs of complement system dysregulation and a high degree of chronic low-grade inflammation. *EClinicalMedicine*. 2022;43:101248.
44. Clarkson-Townsend DA, Douglass AJ, Singh A, et al. Impacts of high fat diet on ocular outcomes in rodent models of visual disease. *Exp Eye Res*. 2021;204:108440.
45. Keeling E, Lynn SA, Koh YM, et al. A high fat "Western-style" diet induces AMD-like features in wildtype mice. *Mol Nutr Food Res*. 2022;66(11):e2100823.
46. Toomey CB, Kelly U, Saban DR, Bowes Rickman C. Regulation of age-related macular degeneration-like pathol-

Investigative Ophthalmology & Visual Science

ogy by complement factor H. *Proc Natl Acad Sci USA*. 2015;112(23):E3040–E3049.

47. Tan BL, Norhaizan ME. Effect of high-fat diets on oxidative stress, cellular inflammatory response and cognitive function. *Nutrients*. 2019;11(11):2579.
48. Nakandakari S, Muñoz VR, Kuga GK, et al. Short-term high-fat diet modulates several inflammatory, ER stress, and apoptosis markers in the hippocampus of young mice. *Brain Behav Immun*. 2019;79:284–293.
49. Zhang X, Li W, Ma Y, et al. High-fat diet aggravates colitis-associated carcinogenesis by evading ferroptosis in the ER stress-mediated pathway. *Free Radic Biol Med*. 2021;177:156–166.
50. Christ A, Lauterbach M, Latz E. Western diet and the immune system: an inflammatory connection. *Immunity*. 2019;51(5):794–811.
51. Chen YH, Huang TY, Lin YT, et al. VPS34 K29/K48 branched ubiquitination governed by UBE3C and TRABID regulates autophagy, proteostasis and liver metabolism. *Nat Commun*. 2021;12(1):1322.
52. Tworak A, Kolesnikov AV, Hong JD, et al. Rapid RGR-dependent visual pigment recycling is mediated by the RPE and specialized Müller glia. *Cell Rep*. 2023;42(8):112982.
53. Tian R, Guo H, Jin Z, et al. Molecular evolution of vision-related genes may contribute to marsupial photic niche adaptations. *Front Ecol Evol*. 2022;10:982073.

Investigative Ophthalmology & Visual Science